Proceedings of ALGORITMY 2024
pp. 139–148

NUMERICAL SIMULATION OF FREEZE/THAW FRONT PROPAGATION IN A SAMPLE OF POROUS MEDIA

MARTIN JEX[1] , MICHAL BENEŠ[1] , MICHAL SNĚHOTA[2] , MARTINA SOBOTKOVÁ[2] , AND JAKUB JEŘÁBEK[2]

Abstract. The freezing of water in porous media depends on various characteristics such as pore size, distribution of grains or boundary conditions. In this contribution we describe a numerical model of freeze/thaw process of a soil sample on the centimeter scale (laboratory sample of repacked sand with relatively low porosity and water) using the finite element method. The model is based on the Štefan problem with a modified latent heat release depending on the water content and is treated in axial symmetry the sample domain. We investigate the sensitivity of this model on initial conditions, material properties and boundary conditions. This contributes to a more profound understanding of freeze/thaw processes observed under laboratory conditions.

Key words. freezing; thawing; finite-element method; porous media; Štefan problem;

1. Introduction. As soil freeze-thaw cycles influence structures, roads, buildings, and other critical infrastructure. They are subject of continuous investigations over more than the last century providing physical formulation [1, 2, 3, 4] and experimental observations [5, 6].

Freezing and thawing in a porous medium is controlled by the heat transfer, mostly between the soil surface and atmosphere. The difference between the specific volume of water and ice causes expansion or shrinkage of pores, leading to the displacement of grains and flow of water between them. Transport through the interface film between ice and grains contributes to additional structural changes. Consequently, the porous medium expands wherever it can, mostly upwards, and creates a variety of surface patterns observable by the naked eye.

In past decades, several modeling approaches have been published in [7, 8, 9, 10] using thermodynamic principles, and taking into account phase transition dynamics and poromechanics.

Recent modeling results are related to specific thermo-hydro-mechanical effects of soil freezing and use currently available numerical methods. Some are partly connected to the multiphysics approach of this article [11, 12, 13, 14]. Optimal adjustment of boundary conditions was investigated in [26, 27]. Very recently [15], the polycrystalline structure of ice in pores was related to the buildup of stresses during soil freezing, whereas the role of solutes during freezing is not yet clarified.

Žák et al. [16] introduced a pore-scale model, assuming geometrically symmetric pores in 2D. A general pore-scale phase-field model of freezing was then introduced in Žák et al. [17] and analyzed in detail in Žák et al. [18]. However, the pore-scale models are impractical for solving large-scale problems due to the computational cost. For the scale studied in this text, the model described in [19] is used, which considers a homogenized medium and the latent heat release is controlled by the water content.

[1]Faculty of Nuclear Sciences and Physical Engineering, Czech Technical University of Prague, Trojanova 13, Praha 2, 120 00, Czech Republic (jexmarti@fjfi.cvut.cz, michal.benes@fjfi.cvut.cz)

[2]Faculty of Civil Engineering, Czech Technical University of Prague, Thákurova 7, 166 29 Praha 6, Czech Republic (michal.snehota@cvut.cz, martina.sobotkova@fsv.cvut.cz, jakub.jerabek@fsv.cvut.cz)

2. Model description. In this section we will introduce the mathematical formulation of equation governing the heat transport and their solution with finite element method. The geometry of the model was motivated by experiments on soil samples performed at the Czech Technical University in Prague, Faculty of Civil Engineering (e.g., see [21]) and is sketched in Section 3.1.

2.1. Conservation of energy. Motivated by the experiment we study the time evolution of temperature T in a domain depicted in Fig. 2.1b. The experimental setup allows to consider the axial symmetry along Γ_6 and use the radial coordinate r and the axial coordinate z.

The volume in a studied apparatus is divided into 3 parts Ω_{GL}, Ω_{PL} and $\Omega_{SS} = \Omega_L \cup \Omega_S \cup \Gamma(t)$. In the parts Ω_{PL} (container) and Ω_{GL} (cover), the heat transfer is described by the heat equation in the coordinates r, z and in time $t \in (0, t_{fin})$

$$\rho_i C_i \partial_t T \quad = \quad \partial_r(k_i \partial_r T) + \frac{1}{r} k_i \partial_r T + \partial_z(k_i \partial_z T), \text{ in } \Omega_i,\ i \in \{PL, GL\} \tag{2.1}$$

where $\rho_i(r, z)$ is density of the material i, $C_i(r, z)$ is the heat capacity of material i, $k_i(r, z)$ is the heat conductivity of the material i, and t_{fin} is the time extent.

The soil sample inside the container is subject of the solid-liquid phase transition. It occurs in soil pores only. Denoting Π_{water}, Π_{ice} liquid and frozen subdomains of a 3D pore, the freezing is described by the Štefan problem (see [22], Sections 6, 10, [23] and references therein)

$$\begin{aligned}
&\rho_j C_j \partial_t T = \nabla(k_j \nabla T) \text{ in } \Pi_j \text{ for } j = \text{water}, \text{ice}, \\
&k_{\text{ice}} \frac{\partial T}{\partial n_{\Gamma(t)}}\bigg|_{\text{ice}} - k_{\text{water}} \frac{\partial T}{\partial n_{\Gamma(t)}}\bigg|_{\text{water}} = L v_{\Gamma(t)}, \text{ on } \Gamma(t) = \partial \Pi_{\text{water}} \cap \Pi_{\text{ice}}, \\
&T - T^* = -\frac{\sigma}{\Delta s} \kappa_\Gamma - \alpha \frac{\sigma}{\Delta s} v_{\Gamma(t)}, \text{ on } \Gamma(t) = \partial \Pi_{\text{water}} \cap \Pi_{\text{ice}},
\end{aligned}$$

where ρ_{water}, ρ_{ice} are density, C_{water} C_{ice} is the heat capacity, k_{water}, k_{ice} is the heat conductivity of water and ice, respectively, Γ is the phase interface, v_Γ its normal velocity, κ_Γ its mean curvature, L is the latent heat, $T^* = 273.15\,\text{K}$ is the ice melting point, σ the surface tension, Δs difference in entropy densities (see Eq. (1.1) in [22]), and α is the kinetic coefficient (see e.g. [23, 18]). As magnitude of the curvature κ_Γ is comparable to magnitude of the curvature in the pore geometry, the phase transition is effectively influenced by complexity of the porous medium and leads to the depression of the melting point denoted as T^D - see [19, 24, 25].

At laboratory-sample or field scales, the heterogeneous structure of porous media is upscaled (homogenized), and described by corresponding conservation laws. In agreement with [20] the co-existence of frozen and liquid phase in the homogenized porous medium is described by the volumetric unfrozen water content given by the power function temperature $\theta(T)$

$$\theta(T) = \begin{cases} \eta & \text{for } T \geq T^D \\ \eta \left| \dfrac{T^D - 273.15}{T - 273.15} \right|^b & \text{for } T < T^D \end{cases}, \tag{2.2}$$

where η is the porosity, and b is an experimentally obtained constant. The function

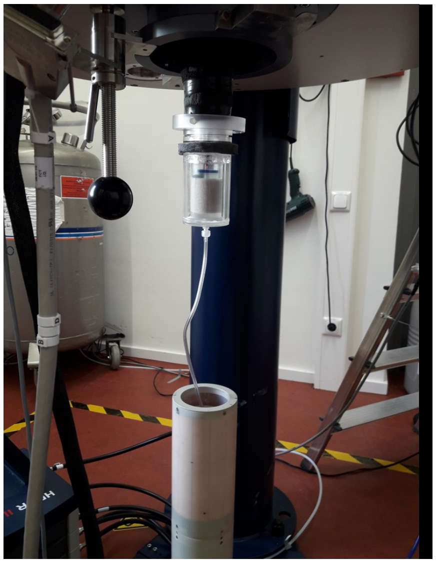

(a) Experimental setup.

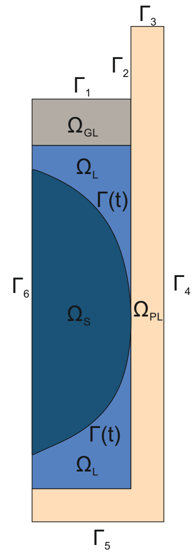

(b) Geometry.

Fig. 2.1: Experimental motivation and geometry notations in axial symmetry.

θ allows to express the enthalpy as

$$\begin{aligned} H(T) &= \int_{T^{min}}^{T} \rho_{SS} C_{SS}\, dv + \eta L \theta(T), \\ \rho_{SS} &= \eta \rho_{\text{grain}} + (1-\eta)\left(\theta \rho_{\text{water}} + (1-\theta)\rho_{\text{ice}}\right), \\ C_{SS} &= \eta C_{\text{grain}} + (1-\eta)\left(\theta C_{\text{water}} + (1-\theta) C_{\text{ice}}\right), \end{aligned}$$

combining the internal energy of the soil sample in Ω_{SS} with the latent heat.

As in [19, 20] we obtain the enthalpy formulation of the Štefan problem in the porous medium sample Ω_{SS}

$$\begin{aligned} \frac{\partial H(T)}{\partial t} &= \partial_r (k_{SS} \partial_r T) + \frac{1}{r} k_{SS} \partial_r T + \partial_z (k_{SS} \partial_z T), \\ k_{SS} &= k_{\text{grain}}^{\eta} \left(k_{\text{water}}^{\theta} k_{\text{ice}}^{1-\theta}\right)^{1-\eta}, \end{aligned} \tag{2.3}$$

in the weak sense (see [19]).

Problem (2.3) is regularized in the ($\epsilon = 10^{-2}$)-neighborhood of T^D, connected to the heat balance in the sample container (2.1) by continuity of temperature and heat flux, written as

$$\frac{\partial H_\epsilon(T)}{\partial t} = \partial_r (k_\epsilon \partial_r T) + \frac{1}{r} k_\epsilon \partial_r T + \partial_z (k_\epsilon \partial_z T) \tag{2.4}$$

in the full setup volume Ω, completed by the initial condition

$$T\Big|_{t=t_0} = T_{\text{ini}} \quad \text{in} \quad \tilde{\Omega},$$

where T_{ini} is the initial temperature of the sample and container, and by the boundary conditions

$$-k_{\Omega_j}\frac{\partial T}{\partial n_{\Gamma_i}} = h_{\Gamma_i}(T - T_{\Gamma_i}), \text{ on } \Gamma_i \times (0, t_{fin}), \quad [i,j] \in B,$$

where $B = \{[1, GL], [2, PL], [3, PL], [4, PL], [5, PL]\}$, k_{Ω_j} is the thermal conductivity of a domain behind the wall Γ_i, h_{Γ_i} is thermal conductivity of the wall i and T_{Γ_i} is temperature on the outside of the wall i.

2.2. Mathematical properties. We briefly summarize the results from [19] useful for the numerical solution by the finite-element method. For $Q = [0, t_{\text{fin}}] \times \Omega$, where Ω describes the experimental setup in the cylindrical symmetry, and the Dirichlet conditions imposed on Ω, the weak formulation is derived by testing problem (2.4) by $v_a \in C^1([0, t_{\text{fin}}]; C_0^\infty(\Omega))$ vanishing for all $t = t_{\text{fin}}$ to obtain

$$0 = \int_Q r(H_\epsilon(T^\epsilon)\frac{\partial}{\partial t}v_a - k_\epsilon \partial_r T^\epsilon \partial_r v_a - k_\epsilon \partial_z T^\epsilon \partial_z v_a)\mathrm{d}r\mathrm{d}z\mathrm{d}t + \int_\Omega H_\epsilon(T_{\text{ini}}(x))v_a(0,x)\mathrm{d}r\mathrm{d}z.$$

The apriori estimates in corresponding spaces allowed to pass to the limit for $\epsilon \to 0$ and to obtain the unique weak solution.

This approach can also be used for the finite element method on a triangular mesh $\mathcal{T}_E$ based on the second order Lagrange elements (global finite element space of second-order polynomials $\mathcal{P}_2^{\mathcal{T}_E}$). Denoting $T^h = \sum_i \overline{T}_i \overline{v}_{T_i}$, with the nodal basis $\{\overline{v}_{T_1}, ..., \overline{v}_{T_{N_E}}\}$ and the nodal solution values $\{\overline{T}_1, ..., \overline{T}_{N_E}\}$, we have

$$\sum_i \left[\frac{\partial \overline{T_i}}{\partial t}\int_{\mathcal{T}_E} rH'_\epsilon(T^{Gal})\overline{v}_{T_i}\overline{v}_{T_j}\mathrm{d}r\mathrm{d}z + \overline{T}_i\int_{\mathcal{T}_E} rk_\epsilon(\partial_r\overline{v}_{T_i}\partial_r\overline{v}_{T_j} + \partial_z\overline{v}_{T_i}\partial_z\overline{v}_{T_j})\mathrm{d}r\mathrm{d}z\right] + \int_{\Gamma_E \cap \mathcal{T}_E} q_T\overline{v}_{T_j}\mathrm{d}S = 0,$$

where $q_T = h_{\Gamma_E}(T - T_{\Gamma_E})$ is the boundary heat flux expression.

3. Computational studies. In this section we discuss the computational model based on the above described approach. We comment on details, such as geometry, material parameters, boundary conditions and assessment of the behavior of the model. All computations were carried out by means of the COMSOL Multiphysics software.

3.1. Case study. This contribution was motivated by the experiment described in [21], in which the sample (Ω_S, Ω_L in Fig. 2.1b) is contained in a dewar flask (Ω_{PL} in Fig. 2.1b). The top of the flask is connected to a top cover by a glass disk (Ω_{GL} in Fig. 2.1b). The temperature on the top (Γ_1 in Fig. 2.1b) of the apparatus is low in the beginning (frozen by the flow of a cooling gas) and increases rapidly after certain time. This reproduces the freeze/thaw cycle. Here, we present a computational model of the experiment along with the parameters used in the computations. Parameters used were fitted to the phenomena observed during the experiment. Sand used in the experiment had the porosity $\eta = 0.3$. The experimental configuration is depicted in the Fig. 2.1a.

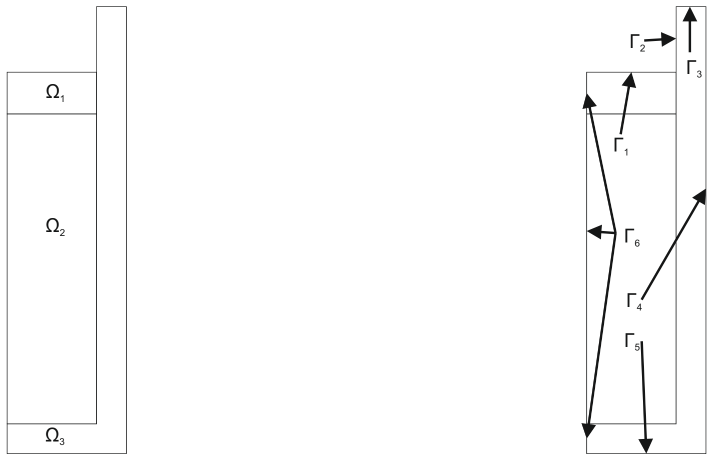

(a) Notation of subdomains. (b) Notation of boundaries.

Fig. 3.1: Geometry of the experimental setup in axial symmetry.

3.2. Geometry and parameters of the model. Due to homogenization at the scale of the experimental configuration, the 3D structure is considered to be axially symmetric. Consequently, the model and its geometry have this nature. In figures, the symmetry axis always is on the left - the line (Γ_6 in Fig. 3.1b).

The geometry Ω of the experimental setup consists of 3 parts abbreviated as Part 1 (Ω_2 in Fig. 3.1a) - the soil sample, Part 2 - the container - the dewar flask made of plexiglass (Ω_3 in Fig. 3.1a), and Part 3 - a glass lens (Ω_1 in Fig. 3.1a) made of laboratory glass. The Newton boundary conditions take into account the heat exchange with the exterior of the sample and the entire experimental setup - the heat can come from the exterior through the sides and bottom part (Γ_3,Γ_4 and Γ_5 in Fig. 3.1b). The boundary conditions on the top (Γ_1 and Γ_2 in Fig. 3.1b) are more challenging since the cooling gas brought to the top of the apparatus varies both in flow and in temperature. Therefore two conditions are used depending on the regime of the experiment. The physical parameters and boundary conditions are summarized in Tab. 3.1 and Tab. 3.2.

3.3. Results. Below, we summarize qualitative and quantitative computational results.

Case 1. This computational study has been performed to simulate a real experiment of a freeze/thaw cycle in the experimental setup shown in Fig. 2.1a. The bottom and side walls are isolated from the exterior by low heat transfer conditions, main heat exchange occurs through the top cap. The model parameters are summarized in Tab. 3.1, the boundary conditions are described in Tab 3.2. Nevertheless, the heat flux along the walls of the experimental apparatus causes the style of freezing recorded in Fig. 3.5. It is consistent with experimental observation.

Case 2. This computational study has been performed to predict the freeze/thaw dynamics in case when main heat exchange with the exterior occurs through the top cap and the bottom part of the apparatus. The model parameters are summarized in Tab. 3.1, the boundary conditions are described in Tab 3.2. Obviously, the dynamics of freezing recorded in Fig. 3.6 differs from Case 1, and is again influenced by the heat flux along the walls of the experimental apparatus.

Parameter	**Region**	**Value**	**Unit**
freezing point depression	Ω_2	-0.1	°C
soil parameter	Ω_2	0.6	1
initial temperature	$\Omega_1, \Omega_2, \Omega_3$	21.4	°C
soil density	Ω_2	1420	$\mathrm{kg/m^3}$
soil thermal conductivity	Ω_2	3.01	$\mathrm{W/(m \cdot K)}$
soil specific heat capacity	Ω_2	1843.38	$\mathrm{J/(kg \cdot K)}$
glass lens density	Ω_1	2450	$\mathrm{kg/m^3}$
glass lens thermal conductivity	Ω_1	1	$\mathrm{W/(m \cdot K)}$
glass lens specific heat capacity	Ω_1	900	$\mathrm{J/(kg \cdot K)}$
plexiglass vessel density	Ω_3	1200	$\mathrm{kg/m^3}$
plexiglass vessel thermal conductivity	Ω_3	0.20	$\mathrm{W/(m \cdot K)}$
plexiglass vessel specific heat capacity	Ω_3	1400	$\mathrm{J/(kg \cdot K)}$

Table 3.1: Parameters for Case 1 and Case 2.

Parameter	**Edge**	**Value** Case 1	**Value** Case 2	**Unit**
External temperature*	Γ_1, Γ_2	-16.40	-16.40	°C
External temperature+	Γ_1, Γ_2	17	17	°C
External temperature*	$\Gamma_3, \Gamma_4, \Gamma_5$	19.50	19.50	°C
External temperature+	$\Gamma_3, \Gamma_4, \Gamma_5$	19.50	19.50	°C
Heat transfer coefficient*	Γ_1, Γ_2	200	30	$\mathrm{W/(m^2 \cdot K)}$
Heat transfer coefficient+	Γ_1, Γ_2	5	5	$\mathrm{W/(m^2 \cdot K)}$
Heat transfer coefficient	Γ_3	5	5	$\mathrm{W/(m^2 \cdot K)}$
Heat transfer coefficient*	Γ_4	2	2	$\mathrm{W/(m^2 \cdot K)}$
Heat transfer coefficient+	Γ_4	2	2	$\mathrm{W/(m^2 \cdot K)}$
Heat transfer coefficient*	Γ_5	2	30	$\mathrm{W/(m^2 \cdot K)}$
Heat transfer coefficient+	Γ_5	2	5	$\mathrm{W/(m^2 \cdot K)}$

Table 3.2: Boundary conditions for Case 1 and Case 2 during the freezing regime * and the thawing regime $^+$.

Mesh dependence. Here, we comment on the the convergence of the numerical solution when the mesh is refined. Four meshes were user for this purpose, as shown in Fig. 3.2. The *Coarsest mesh* consists of 141 elements (triangles) and is generated with the following parameters: maximum element size scaling factor is 1.5, element growth rate is 1.4, mesh curvature factor is 0.4, mesh curvature cutoff is 0.005, and resolution in narrow regions is 1. The *Coarser*, *Finer* and *Finest* meshes were obtained by subsequent bisection of the boundaries of the elements of the preceding mesh. The numerical solutions computed on these meshes were compared visually at a selected time moment. For *Case 1* at $t = 16000[\mathrm{s}]$, the temperature field in color scale is compared in Fig. 3.3. The position of the temperature isoline $T = T^D$ indicates consistency of these results. For *Case 2* at $t = 15000[\mathrm{s}]$, the *Finer* and *Finest* mesh are close each to other whereas other meshes exhibit a delay in the freezing front propagation.

4. Conclusion. A computational model of the freeze/thaw laboratory experiments based on the finite-element method was presented. It allows the parameter optimization, adjustment of boundary conditions and complex geometry of the ex-

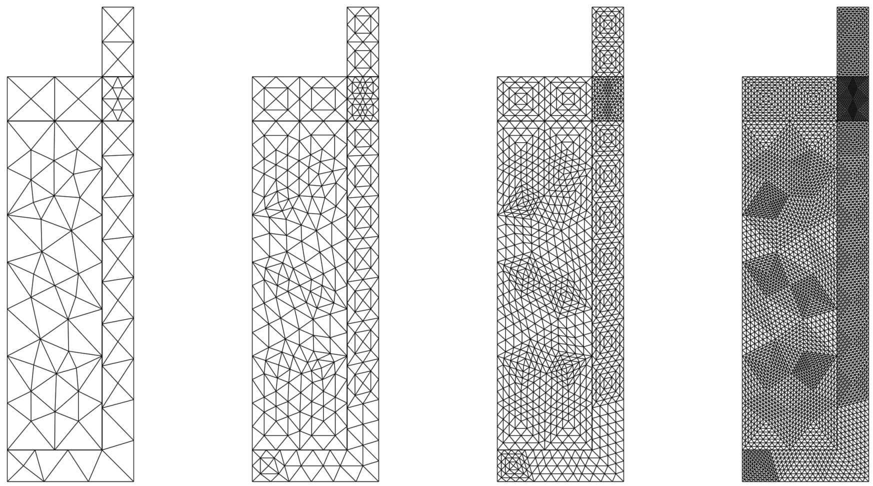

(a) Coarsest mesh (b) Coarser mesh (c) Finer mesh (d) Finest mesh

Fig. 3.2: Finite-element meshes used for comparison.

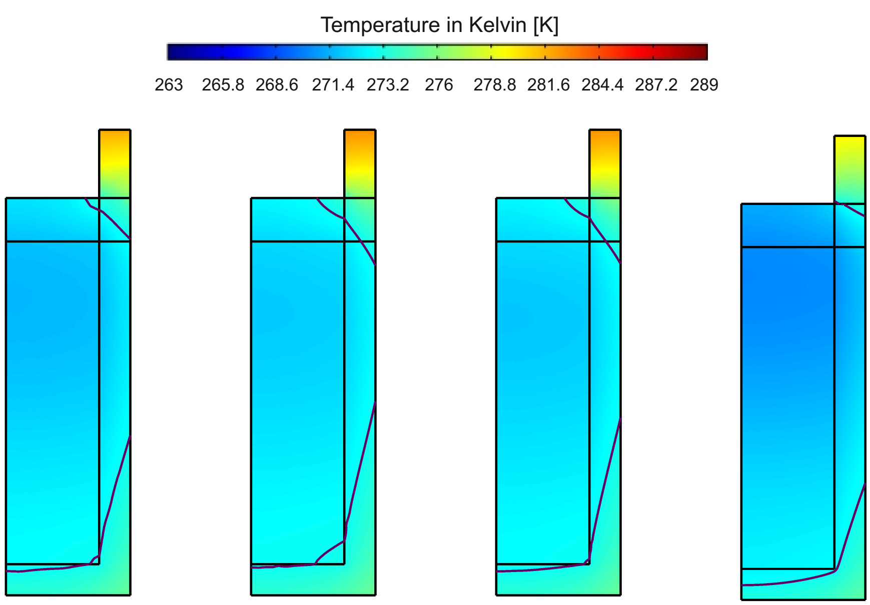

(a) Coarsest mesh (b) Coarser mesh (c) Finer mesh (d) Finest mesh

Fig. 3.3: **Case 1** on different meshes at time 16000 [s], purple line signifies where $T = T^D$.

perimental setup. Future development of the model will be focused on structural dynamics generated by the difference in specific volume between water and ice.

Acknowledgments. The research was partly supported by the project No. 21-09093S of the Czech Science Foundation, and by the project No. SGS23/188/OHK4/3T/14 of the Student Grant Agency of the Czech Technical University in Prague.

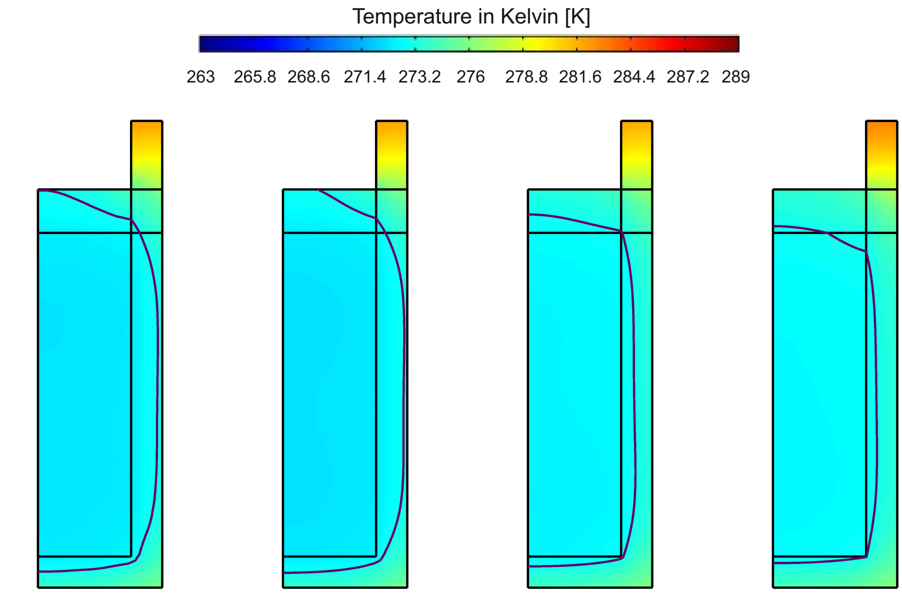

(a) Coarsest mesh (b) Coarser mesh (c) Finer mesh (d) Finest mesh

Fig. 3.4: **Case 2** on different meshes at time 15000[s], purple line signifies where $T = T^D$.

REFERENCES

[1] Taber S., *The mechanics of frost heaving*, The Journal of Geology, Volume 38, pp. 303–317, 1930.

[2] Guymon G.L., Berg R.L., and Hromadka T.V., *Mathematical model of frost heave and thaw settlement in pavements*, CRREL report ; 93-2, Hanover, 1993.

[3] Nikolaev P., Jivkov A.P., Margetts L., and Sedighi M., *Non-local modelling of freezing and thawing of unsaturated soils*, Advances in Water Resources, Volume 184, 104614, 2024.

[4] Lu B.Q., et al., *Cooling and wetting of soil decelerated ground freezing-thawing processes of the active layer in Xing'an permafrost regions in Northeast China*, Advances in Climate Change Research, Volume 14, pp. 126-135, 2023.

[5] Furuzumi M., et al., *Thermal and freezing strains on a face of wet sandstone samples under a subzero temperature cycle*, Journal of Thermal Stresses, Volume 27, pp. 331–344, 2004.

[6] Gens A., *Soil-environment interactions in geotechnical engineering*, Géotechnique, Volume 60(1), pp. 3–74, 2010.

[7] Li J., et al., *Modeling permafrost thaw and ecosystem carbon cycle under annual and seasonal warming at an arctic tundra site in Alaska*, Journal of Geophysical Research: Biogeosciences, Volume 119, Issue 6, pp. 1129–1146, 2014.

[8] Coussy O., *Poromechanics of freezing materials*, Journal of the Mechanics and Physics of Solids, Volume 53, pp. 1689–1718, 2005.

[9] Nishimura S., Gens A., Olivella S., and Jardine R.J., *THM-coupled finite element analysis of frozen soil: formulation and application*, Géotechnique, Volume 59, Issue 3, pp. 159–171, 2009.

[10] Mikkola M., and Hartikainen J., *Mathematical model of soil freezing and its numerical implementation*, International Journal for Numerical Methods in Engineering, Volume 52, pp. 543–557, 2001.

[11] Lei D., Yang Y., Cai C., Chen Y., and Wang S., *The Modelling of freezing process in saturated soil based on the thermal-hydro-mechanical multi-physics field coupling theory*, Water, Volume 12, 2684, 2020.

[12] Sweidan A.H., Heider Y., and Markert B, *A unified water/ice kinematics approach for phase-field thermo-hydro-mechanical modeling of frost action in porous media*, Computer Methods in Applied Mechanics and Engineering, Volume 372, 113358, 2020.

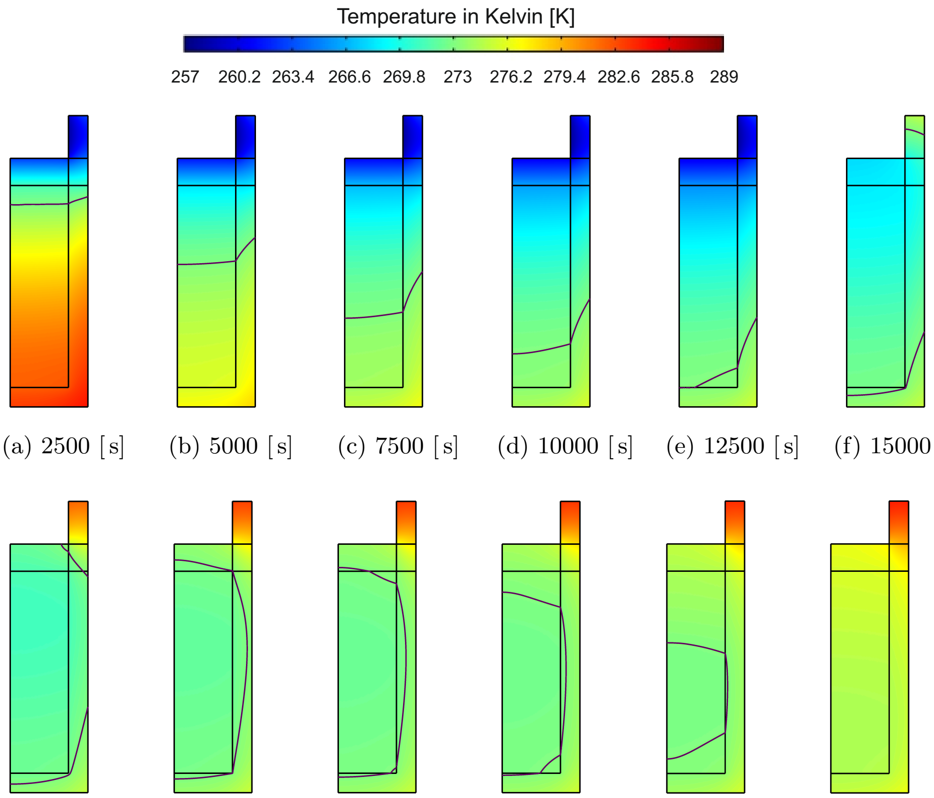

(a) 2500 [s] (b) 5000 [s] (c) 7500 [s] (d) 10000 [s] (e) 12500 [s] (f) 15000 [s]

(g) 17500 [s] (h) 20000 [s] (i) 21000 [s] (j) 22000 [s] (k) 23000 [s] (l) 24000 [s]

Fig. 3.5: **Case 1.** Freeze/thaw cycle captured at different times levels. The purple contour indicates the position of the temperature isoline $T = T^D$.

[13] Sweidan A.H., Niggemann K., Heider Y., Ziegler M., and Markert B., *Experimental study and numerical modeling of the thermo-hydro-mechanical processes in soil freezing with different frost penetration directions*, Acta Geotechnica, Volume 17, pp. 231–255, 2022.

[14] Suh H.S., and Sun W.C., *Multi-phase-field microporomechanics model for simulating ice-lens growth in frozen soil*, International Journal for Numerical and Analytical Methods in Geomechanics, Volume 46, Issue 12, pp. 2307–2336, 2022.

[15] Gerber D., Wilen L.A., Dufresne E.R., and Style R.W., *Polycrystallinity enhances stress buildup around ice*, Physical Review Letters, Volume 131, 208201, 2023.

[16] Žák A., Beneš M., and Illangasekare T.H. and Trautz A.C., *Mathematical model of freezing in a porous medium at micro-scale*, Communications in Computational Physics, Volume 24, Issue 2, pp. 557–575, https://doi.org/10.4208/cicp.OA-2017-0082, 2018.

[17] Žák A., and Beneš M., *Micro-scale model of thermomechanics in solidifying saturated porous media*, Acta Physica Polonica A., Volume 134, Issue 3, pp. 678-682, https://doi.org/10.12693/APhysPolA.134.678, 2018.

[18] Žák A., Beneš M., and Illangasekare T.H., *Pore-scale model of freezing inception in a porous medium*, Computer Methods in Applied Mechanics and Engineering, Volume 414, 116166, https://doi.org/10.1016/j.cma.2023.116166, 2023.

[19] Žák A., Beneš M., and Illangasekare T. H., *Analysis of model of soil freezing and thawing*, IAENG International Journal of Applied Mathematics, Volume 43, Issue 3, pp. 127–134, September 2013.

[20] Nicolsky D. J., Romanovsky V. E., and Panteleev G. G., *Estimation of soil thermal properties using in-situ temperature measurements in the active layer and permafrost*, Cold Regions Science and Technology, Volume 55, pp. 120–129, 2009.

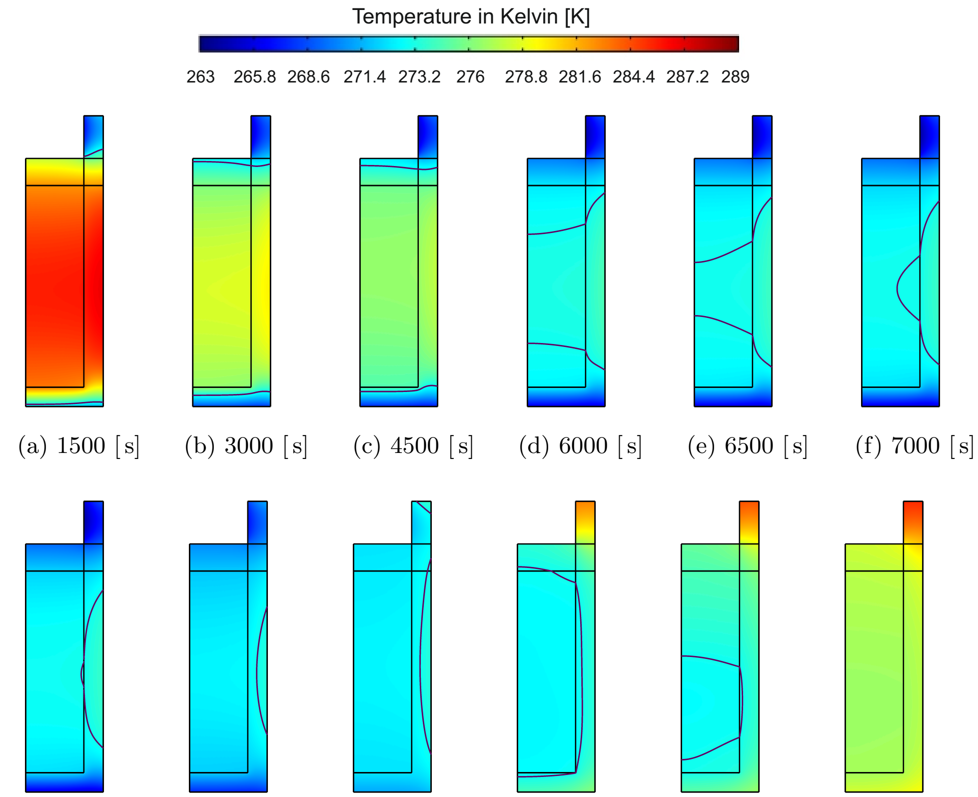

(a) 1500 [s] (b) 3000 [s] (c) 4500 [s] (d) 6000 [s] (e) 6500 [s] (f) 7000 [s]

(g) 7500 [s] (h) 12000 [s] (i) 13500 [s] (j) 15000 [s] (k) 16500 [s] (l) 18000[s]

Fig. 3.6: **Case 2.** Freeze/thaw cycle captured at different times levels. The purple contour indicates the position of the temperature isoline $T = T^D$.

[21] Sklenář J., *Magnetic resonance imaging of freezing and thawing of water in porous media*, Master Thesis, Czech Technical University in Prague, Faculty of Civil Engineering, 2022.

[22] Gurtin M.E., *On the two-phase Stefan problem with interfacial energy and entropy*, Archive for Rational Mechanics and Analysis, Volume 96, pp. 199-241, 1986.

[23] Schmidt A., *Computation of three dimensional dendrites with finite elements*, Journal of Computational Physics, Volume 125, pp. 293-312, 1996.

[24] Michalowski R.L., and Zhu M., *Frost heave modelling using porosity rate function*, The International Journal for Numerical and Analytical Methods in Geomechanics, Volume 30, pp. 703-722, 2006.

[25] Liu Z., Muldrew K., Wan R.G., and Elliott J.A., *Measurement of freezing point depression of water in glass capillaries and the associated ice front shape*, Physical review. E, Statistical, nonlinear, and soft matter physics, Volume 67(6 Pt 1), 061602, 2003.

[26] Wodecki A., Strachota P., Oberhuber T., Škardová K., Balázsová M., and Bohatý M., *Numerical optimization of the Dirichlet boundary condition in the phase field model with an application to pure substance solidification*, Computers & Mathematics with Applications, Volume 145, pp. 90-105, 2023.

[27] Wodecki A., Balázsová M., Strachota P., and Oberhuber T., *Existence of optimal control for Dirichlet boundary optimization in a phase field problem*, Journal of Dynamical and Control Systems, Volume 29, pp. 1425-1447, 2023.